scientific reports

Check for updates

OPEN

Predicting EMI in UAVs using characteristic mode analysis: a case study of the DJI Phantom 4

Zeinab Jalali[1], Seyed Mohamad Hashemi[1]✉, Alireza Sadeqi[1], V. Mashayekhi[2] & Javad Ghalibafan[2]

Unmanned aerial vehicles (UAVs) are increasingly utilized across various sectors, particularly in Internet of Things (IoT) applications. However, their susceptibility to electromagnetic interference (EMI) poses significant challenges to operational performance. This study assesses the susceptibility of a DJI Phantom 4 UAV to EMI using Characteristic Mode Analysis (CMA) and experimental validation. Unlike prior studies that focus on simplified UAV models, this research incorporates all subsystems to enhance CMA accuracy. By extending the analysis over a wide frequency range, it identifies components with high induced currents and demonstrates that UAVs are more susceptible to interference at higher frequencies. Experimental validation further confirms the EMI-induced failure risks of these components, highlighting the importance of structural details in electromagnetic assessments. Subsequent experimental testing assessed which of these components were most vulnerable to EMI-induced damage. Findings reveal that long power supply wires, particularly those connecting motors to ESC boards, exhibit the highest susceptibility. The results underscore the necessity of shielding power supply cables, akin to coaxial cable design, to enhance the UAV's electromagnetic resilience. These insights provide applicability across a range of UAV designs, facilitating improved performance in electromagnetically dense environments.

Unmanned Aerial Vehicles (UAVs) are increasingly vital across various sectors, including aerial photography, agriculture, infrastructure inspection, and search and rescue operations. Beyond these applications, UAVs represent a practical and efficient embodiment of the IoT, offering a viable alternative to traditional, labor-intensive methods for inspecting critical infrastructure, such as power transmission lines, base stations, and radio transmission towers. By leveraging advanced technologies, UAVs significantly reduce the need for human resources in routine maintenance tasks, thereby enhancing the reliability and safety of essential infrastructure systems[1].

Despite these advantages, UAVs face significant operational challenges, particularly their susceptibility to EMI[2]. According to the DJI Phantom 4 user manual[3], it is crucial to avoid operating near high-voltage power lines and areas with elevated electromagnetic activity to minimize the risk of interference. Modeling coupled currents in UAV wiring and electronics due to EMI presents significant challenges. Studies typically focus on a simplified UAV model, conducting numerous simulations and measurements to assess the induced currents under various conditions and environments[4–6]. However, these approaches do not capture the full electromagnetic behavior of UAVs in real-world scenarios, where multiple subsystems and their interactions play a critical role in EMI susceptibility.

The coupled currents within a UAV can vary significantly based on its orientation relative to the incident electromagnetic field's direction, polarization, and frequency[4,6].Current methodologies for Electromagnetic Compatibility (EMC) testing rely heavily on extensive experimental validation, which is often time-consuming and resource-intensive[7]. CMA offers an efficient alternative for predicting and quantifying EMI effects by identifying the dominant resonant modes that contribute to electromagnetic coupling[8]. By applying CMA, researchers can more accurately target their experimental measurements, reducing the need for exhaustive testing while still ensuring that all critical EMI interactions are thoroughly analyzed.

CMA has been instrumental in optimizing antenna designs, providing deep insights into the modal behavior of electromagnetic structures. This method enables systematic enhancements to antenna performance parameters, allowing for efficient adjustments to dimensions and structures based on modal analysis[9–15]. The original concept of characteristic modes was first introduced in 1965 to analyze electromagnetic scattering, treating obstacles as parasitically excited antennas with virtual terminals. This approach enables a deeper understanding of resonance

[1]Faculty of Electrical Engineering, Shahid Rajaee Teacher Training University, Tehran, Iran. [2]Department of Electrical Engineering, Shahrood University of Technology, Shahrood, Iran. ✉email: sm.hashemi@sru.ac.ir

phenomena, as characteristic modes are inherently linked to an object's shape and influence field interactions[16]. This concept later extended using the Method of Moments (MoM), which facilitated the practical computation of CMA for complex electromagnetic structures[8,17]. Since its introduction, CMA has become a powerful tool for solving complex electromagnetic problems, evolving beyond its initial focus on perfect electric conductors to incorporate dielectric bodies[18,19]. These advancements have significantly expanded its utility in areas such as reconfigurable antennas[15] achieved frequency tunability, while improved MIMO performance[20] by reducing envelope correlation. CM-based loading strategies enhanced bandwidth in[21,22] demonstrated multi-resonant small antennas. Mutual coupling mitigation in MIMO systems was addressed in[23], with[24] further optimizing wideband performance. This study leverages CMA to analyze electromagnetic coupling and interference in UAV structures, providing deeper insights into EMI effects across all UAV's subsystems.

Previous studies[25–29] have often relied on simplified UAV models comprising four wires attached to a square metallic patch that do not account for the full range of subsystems comprising a UAV. Such models, while useful for certain analyses, fail to capture the complexity and interactions between various components that significantly influence a UAV's electromagnetic behavior.

This study extends the application of CMA to UAV EMI analysis by considering all major subsystems of the DJI Phantom 4, including the GPS module, motors, ESC boards, antennas, and other electronic components. Unlike previous research, which focuses on single-component interactions, this work evaluates the cumulative effects of EMI on an entire UAV system. Additionally, while prior studies applied CMA to UAVs in a narrowband approach, this work extends the analysis over a wide frequency range, demonstrating that UAVs are more susceptible to interference at higher frequencies. Another novel contribution is the statistical analysis performed. The analysis is structured in three stages: the first stage examines the UAV's primary structure, the second stage incorporates key electronic components, and the final stage includes all subsystems to provide a complete electromagnetic representation.

CMA is applied to analyze and mitigate the susceptibility of quadcopter UAVs to EMI. Initially, the fundamental modes of the proposed UAV model are determined and analyzed. By understanding these modes, the behavior of coupled currents induced at various locations on the UAV structure, when subjected to plane wave excitations, is predicted across a range of frequencies and incident directions. The calculated modes serve as critical reference points for understanding how electromagnetic fields interact with the UAV. By identifying the specific modes that resonate at given frequencies and directions, it becomes possible to predict the resulting electromagnetic coupling at different points on the UAV.

This approach allows for a more accurate identification of EMI-vulnerable regions and offers valuable insights into potential vulnerabilities mitigation strategies. By integrating CMA simulations with experimental validation, this research bridges the gap between theoretical predictions and real-world EMI effects on UAVs. The findings highlight the importance of shielding strategies, particularly for power supply cables, and provide recommendations for improving UAV electromagnetic resilience. This study contributes to the broader field of UAV electromagnetic compatibility and serves as a foundation for future investigations into EMI mitigation techniques.

The structure of the study is outlined as follows: Section II presents the UAV subsystem analysis using CMA, detailing the three-stage modeling approach. Section III evaluates the UAV's electromagnetic behavior through CMA, identifying resonant modes. Section IV validates the CMA results through full-wave simulations. Section V analyzes UAV subsystem sensitivity using modal significance and surface current distribution. Section VI describes the experimental validation of UAV electromagnetic susceptibility. Finally, Section VII summarizes the conclusions and discusses implications for UAV electromagnetic resilience.

UAV subsystem analysis using CMA

Previous studies primarily analyzed the UAV's overall structure, often relying on simplified models that omit subsystem interactions[9–11]. This study addresses that limitation by considering the complete UAV architecture, enabling a more precise evaluation of EMI susceptibility. Compared to conventional full-wave solvers and circuit-based approaches, CMA offers computational efficiency and deeper physical insights by decomposing electromagnetic fields into characteristic modes. This enables a systematic analysis of EMI coupling mechanisms across UAV subsystems. By decomposing complex electromagnetic fields into characteristic modes, CMA provides detailed insights into how these fields interact with the UAV structure. This method allows for the identification of specific frequencies and modes that may cause detrimental interference, thereby revealing potential vulnerabilities.

The analysis is structured in three stages, each progressively integrating more subsystems to assess their impact on the UAV's electromagnetic behavior. In the initial stage, a simplified model, depicted in Fig. 1(a), containing only the primary components—motors, battery, mainboard, electronic speed controller boards, and power interface module—is analyzed. This baseline configuration isolates the influence of core components on electromagnetic interference and compatibility characteristics, offering a foundational understanding of the UAV's electromagnetic response.

In the second stage, additional subsystems are incorporated into the analysis, including the GPS board and cover, LED sensors, vision sensors, flight controller, ultrasonic module, gimbal mainboard, and gimbal power board. This expanded configuration, shown in Fig. 1(b), allows for an assessment of the impact of these additional components on the UAV's electromagnetic performance.

The final stage integrates all subsystems of the DJI Phantom 4, including the camera speed controller board, pitch, roll, and yaw motors, IMU board, camera board, camera mainboard, and antennas, as shown in Fig. 1(c). This comprehensive model provides a complete representation of the UAV, facilitating a thorough simulation and analysis of its electromagnetic compatibility.

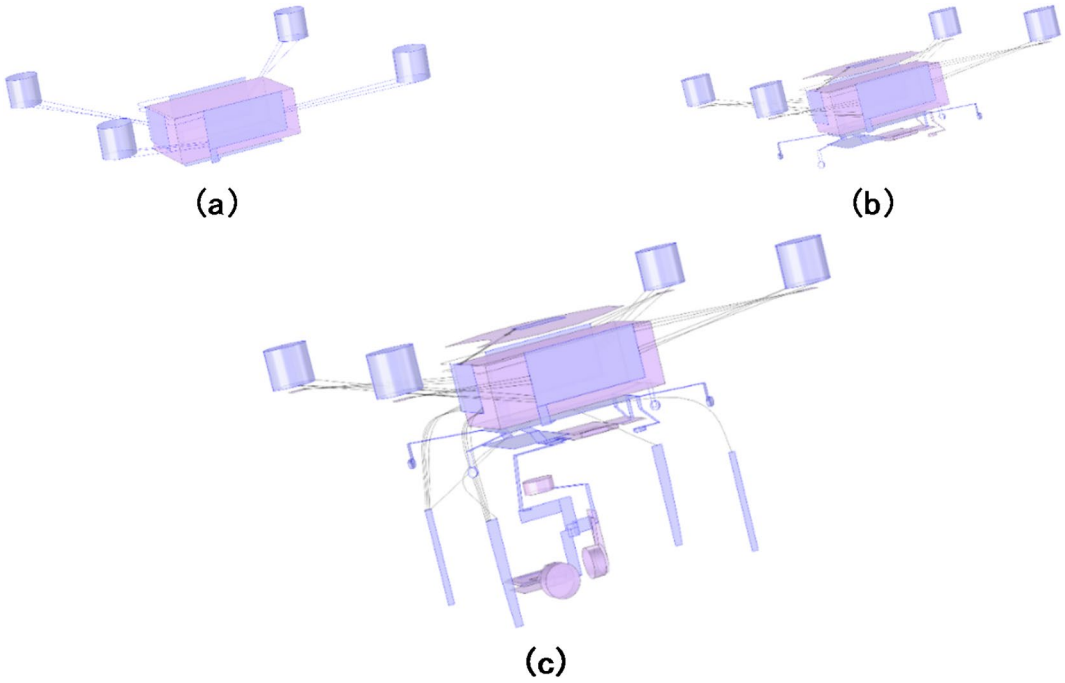

Fig. 1. The Frame Model of DJI Phantom 4 UAV (a) main subcomponents, (b) more subcomponents, (c) all subcomponents considered.

The primary objective is to determine whether including each subsystem individually yields more precise results and to understand their overall impact on the UAV's electromagnetic performance. By comparing the outcomes from the simplified, intermediate, and complete models, the significance of each subsystem's contribution to electromagnetic interference and compatibility is assessed. This methodical approach offers deeper insights into optimizing UAV design for enhanced electromagnetic resilience.

CMA evaluation of UAV electromagnetic behavior

CMA was employed to calculate the fundamental modes of the UAV structure, predicting its response to various electromagnetic excitations. The CMA results, shown in Fig. 2, were plotted across the frequency range of 200 to 400 MHz, focusing on the modal significance of the first ten modes in three distinct UAV configurations. The analysis revealed distinct resonant frequencies for each configuration, demonstrating how the inclusion of different subsystems influences the UAV's electromagnetic behavior.

In the first stage, where only the primary structure of the UAV was analyzed, modes 1, 2, and 4 exhibited resonance at 240, 262, and 280 MHz, respectively. This initial configuration provided a baseline understanding of the UAV's modal behavior, with minimal complexity due to the absence of additional subsystems. The second stage incorporated subsystems such as the GPS board, LED sensors, vision sensors, flight controller, ultrasonic module, and gimbal boards. In this configuration, modes 1–4 and 8 resonated at frequencies of 240, 260, 325, 270, and 400 MHz, respectively. The inclusion of these subsystems altered the resonant frequencies and increased the complexity of the modal behavior. The final stage involved the complete configuration of the DJI Phantom 4, including all structural and electronic subsystems. In this comprehensive model, modes 1–4 and 8–10 resonated at frequencies of 230, 239, 258, 270, 278, 290, and 303 MHz, respectively. This configuration exhibited a higher number of resonant modes, indicating more intricate electromagnetic interactions within the fully assembled UAV.

A key factor influencing mode variation in the complete UAV configuration is the increased coupling between the subsystems. The presence of additional conductive elements, affects the distribution of induced currents, altering modal behavior. The expansion of resonant modes in Stage 3 can be attributed to the structural complexity and interconnections between subsystems, which introduce additional resonances due to secondary coupling effects.

The results demonstrate that as more subsystems are integrated into the model, the number of resonant modes increases, leading to a more detailed and accurate representation of the UAV's electromagnetic characteristics.

This comprehensive approach highlights the necessity of including all subsystems in the analysis to obtain precise and reliable results. Subsequent sections will focus on simulations and analyses based on the complete UAV configuration as defined in the third stage. The insights derived from this detailed model emphasize the critical importance of subsystem inclusion for accurate electromagnetic compatibility assessments in UAVs.

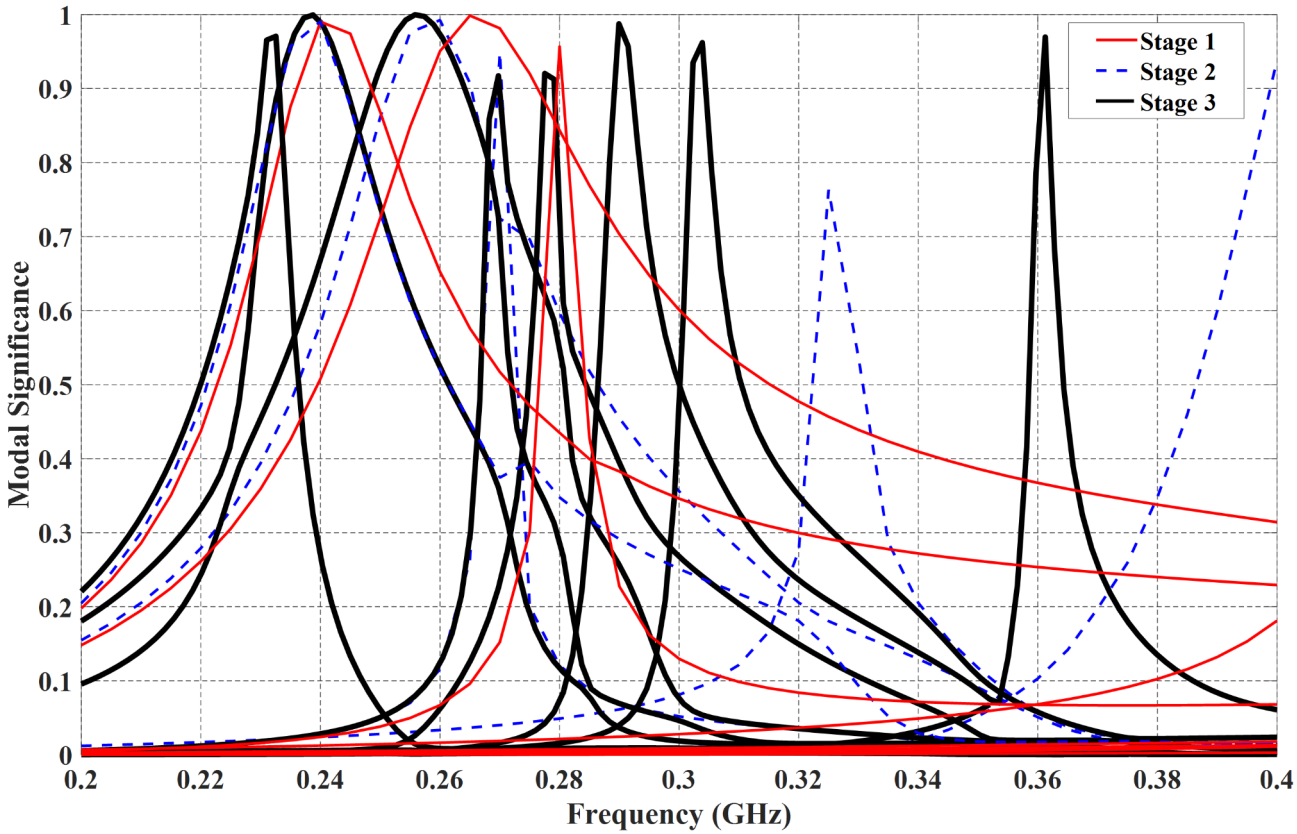

Fig. 2. Modal significance of the first 10 modes of the Phantom 4 UAV model in Fig. 1. Red, blue, and black lines respectively represent modes of Fig. 1. (a), (b), and (c).

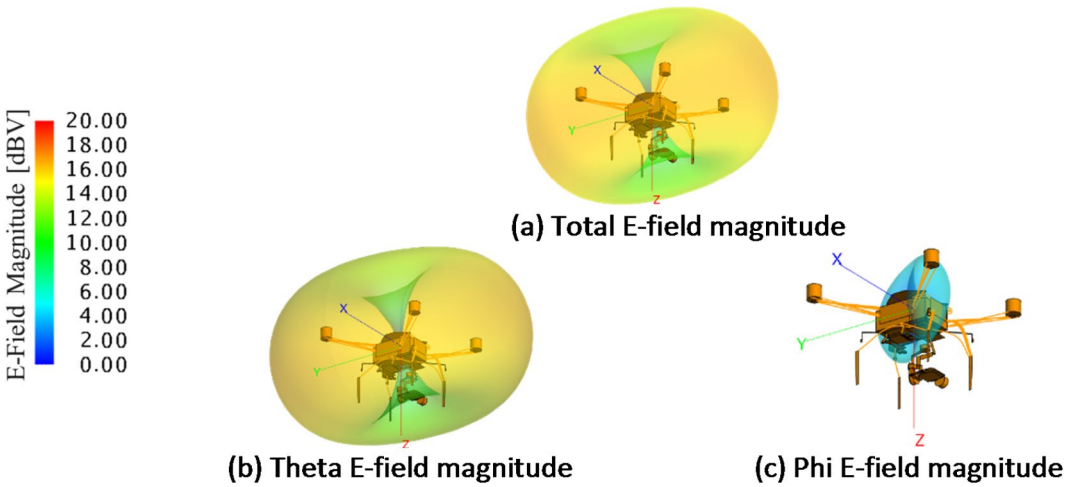

Fig. 3. The radiation pattern of the Phantom 4 UAV model stage 3 is plotted at the resonance frequency of mode 1.

Validation and simulation of CMA results for UAV

In this study, the impact of electromagnetic waves on the DJI Phantom 4 UAV frame was analyzed using Characteristic Mode Analysis (CMA). The fully configured structure, including all subsystems of the Phantom 4, was simulated using the FEKO[30] 2023 software, as depicted in Fig. 1(c). The radiation pattern for the first resonant mode was plotted, showing the Total E-field magnitude, Theta E-field magnitude, and Phi E-field magnitude, as illustrated in Fig. 3. The results indicate that the structure experiences maximum impact when the electromagnetic wave is incident with a Theta polarization at angles of $\theta = 90^\circ$ & $\phi = 90^\circ$ or $\theta = 90^\circ$ & $\phi = 0^\circ$.

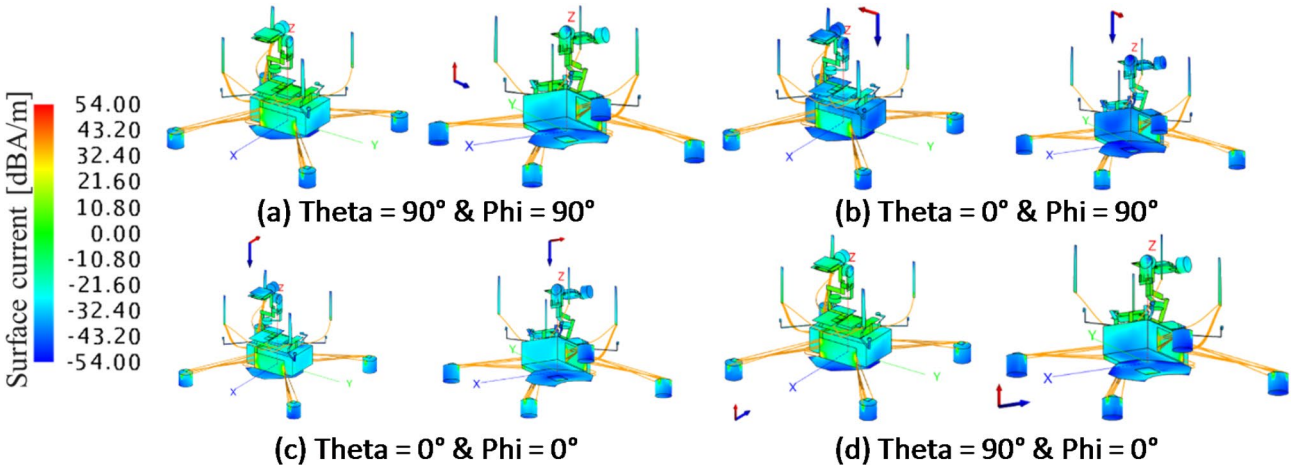

Fig. 4. Plane wave at theta polarization at the resonance frequency of mode 1 (232 MHz) at different angles of incidence θ and ϕ.

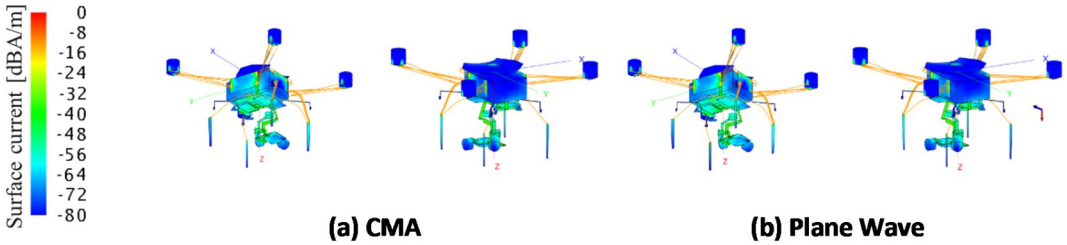

Fig. 5. Comparison between the normalized coupled current to the Phantom 4 UAV model (a) CMA, (b) Plane wave at the resonance frequency of mode 1 (232 MHz), and polarization due to an incident wave at $\theta = 90^\circ$ & $\phi = 90^\circ$.

To validate these findings, plane waves were incident on the structure from various directions using the full-wave Method of Moments (MoM) solver in FEKO[30] 2023, and the surface currents on the structure were analyzed, as shown in Fig. 4. The surface current patterns confirm that the maximum surface current occurs when the plane wave is incident with Theta polarization at angles $\theta = 90^\circ$ & $\phi = 90^\circ$ or $\theta = 90^\circ$ & $\phi = 0^\circ$.

Achieving a comprehensive understanding of the sensitivity of all UAV subsystems across a broad frequency range and multiple modes typically requires extensive simulations involving numerous incident plane waves. However, this process can be computationally intensive and time-consuming. CMA offers a more efficient alternative by significantly reducing the number of required simulations while maintaining high reliability. CMA enables the prediction of system behavior across various frequencies and modes, providing valuable insights with fewer computational resources.

To ensure the accuracy of the CMA analysis, the DJI Phantom 4 UAV frame was simulated using CMA in the FEKO[30] 2023 software, and the surface currents were plotted. Subsequently, a full-wave simulation was conducted at the same frequency and mode, and the surface currents were again plotted. As shown in Fig. 5, the normalized currents from both the CMA and full-wave simulations exhibit a high degree of correlation. This strong agreement validates the accuracy of the CMA method. Consequently, subsequent simulations in this study were conducted using the CMA approach.

The results demonstrate the reliability of CMA in predicting the electromagnetic response of the UAV structure. By employing CMA, it is possible to analyze the structure at different frequencies and identify the most sensitive subsystems to electromagnetic interference. This comprehensive analysis supports the enhancement of UAV design and operational safety in environments with high electromagnetic interference.

To conduct a detailed analysis using CMA, the evaluation of modal significance and surface currents is essential. Both $\boldsymbol{MS_n}$ and $\boldsymbol{J_n}$ are intrinsic properties of the system and are not influenced by external incident fields, making them fundamental for understanding and predicting system behavior across various electromagnetic environments.

Modal Significance $(\boldsymbol{MS_n})$: $\boldsymbol{MS_n}$ quantifies the relative contribution of a particular mode to the total coupled current and is independent of the excitation source. It reaches its maximum value when the mode is resonant, providing crucial insight into which modes dominate at a given frequency. $\boldsymbol{MS_n}$ can be calculated as:

$$MSn = \frac{1}{|1 + j\lambda_n|} \tag{1}$$

Where λ_n represents the eigenvalue of the mode. MS_n achieves its maximum value of 1 when $\lambda_n = 0$, indicating resonance. By comparing MS_n values across different modes at any frequency, it becomes possible to identify which modes predominantly influence the coupled current.

Surface Currents (J_n): J_n describes the current distribution for each mode, highlighting areas of maximum and minimum current within the system. By examining J_n, it is possible to determine how different modes contribute to the overall current distribution on the UAV components. This analysis provides detailed insights into the electromagnetic behavior of complex structures, enabling precise modeling and optimization of their electromagnetic properties[7,8].

In this study, the UAV frame's surface current distribution was analyzed to identify the most vulnerable subsystems to EMI. The results indicate that certain UAV subsystems, such as the power interface module and GPS board, exhibit significant coupled currents at specific resonant frequencies. Additionally, it was observed that subsystems with long interconnecting wires, particularly the motor-ESC wiring, are more susceptible to EMI.

The findings from CMA provide valuable guidelines for UAV design improvements, particularly in EMI-prone environments. The results suggest that shielding long power supply cables, adopting differential signal transmission cables (like flat cables) for critical sensor subsystems could significantly enhance electromagnetic resilience in UAVs.

Evaluating UAV subsystem sensitivity using modal significance and surface current analysis

The primary objective of this study is to assess the susceptibility of all subcomponents of the DJI Phantom 4 UAV frame to electromagnetic waves, with the goal of enhancing the UAV's performance in electromagnetically dense environments. CMA was selected due to its accuracy and computational efficiency in identifying resonant frequencies and coupled currents.

Initially, the validity of the CMA approach was confirmed through comparative analysis with full-wave simulations. The UAV frame was then simulated using the full-wave solver FEKO[30] 2023 over a frequency range of 200 MHz to 5 GHz. Figure 6 presents the modal significance MS_n of the first ten modes, demonstrating that higher frequencies result in a greater number of resonant modes, indicating increased EMI susceptibility.

Understanding these sensitivities is crucial for optimizing UAV design to minimize electromagnetic interference and ensure reliable operation.

At the resonant frequency of each mode, the J_n and associated radiation patterns were analyzed, as shown in Fig. 7, and 8. These visualizations help identify which subcomponents experience higher induced currents.

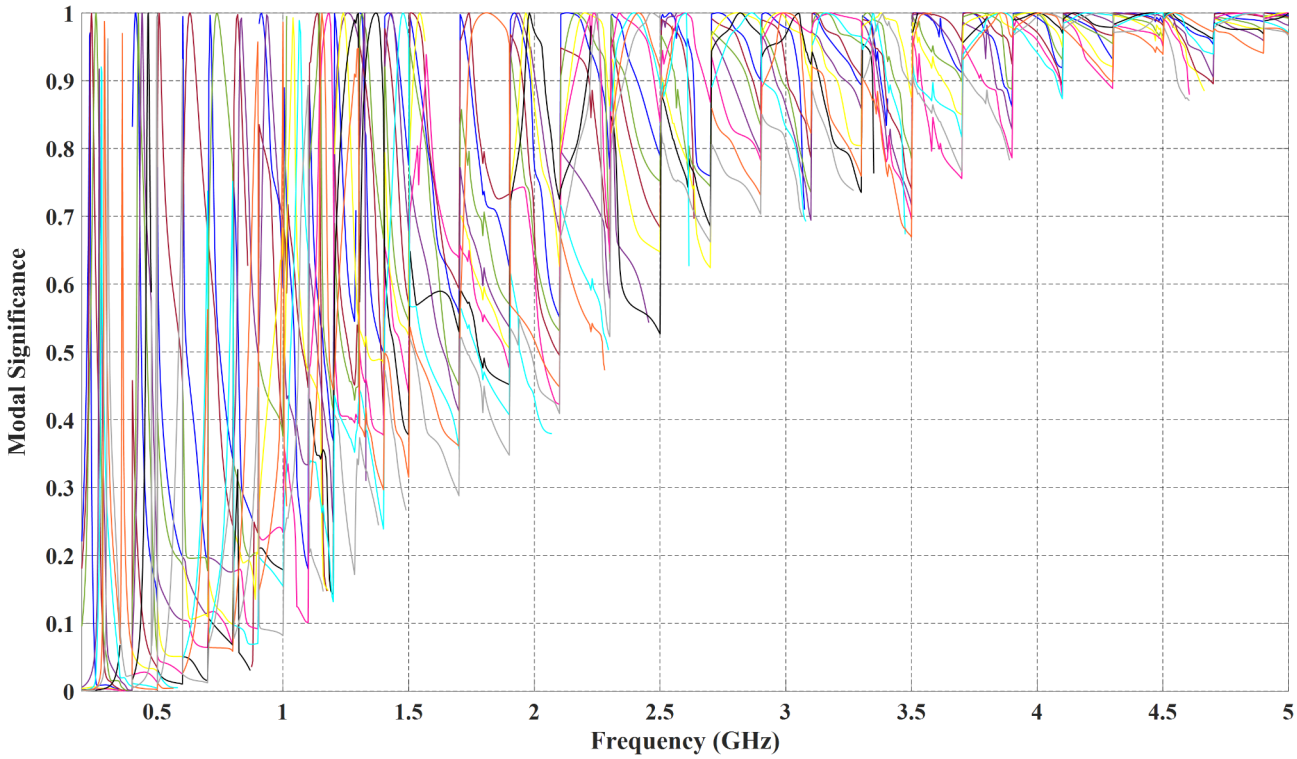

Fig. 6. Modal significance of the first 10 modes of the Phantom 4 UAV model.

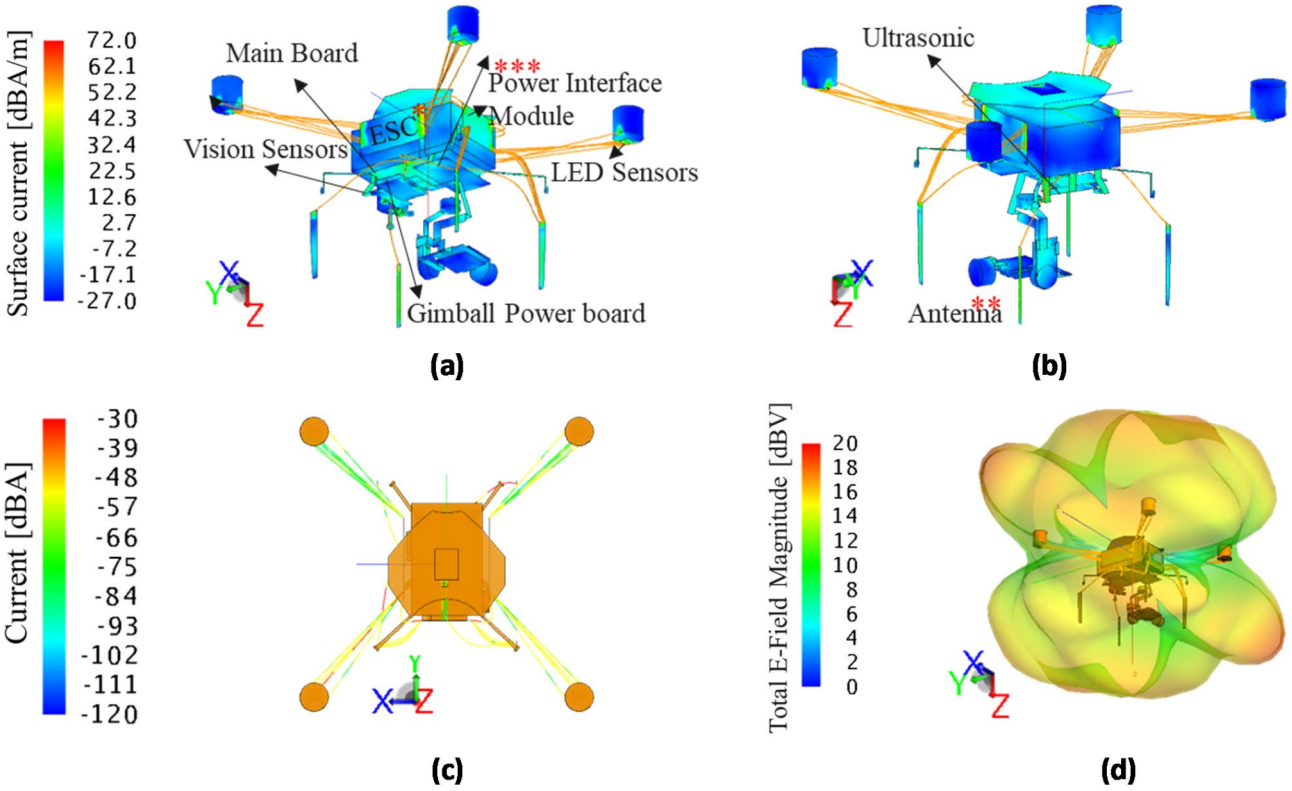

Fig. 7. Surface-current distribution of Mode 9 of the Phantom 4 UAV structure at: 2.41 GHz (a) view 1, (b) view 2, (c) coupled current to the wires, and (d) The radiation pattern of total E-field magnitude.

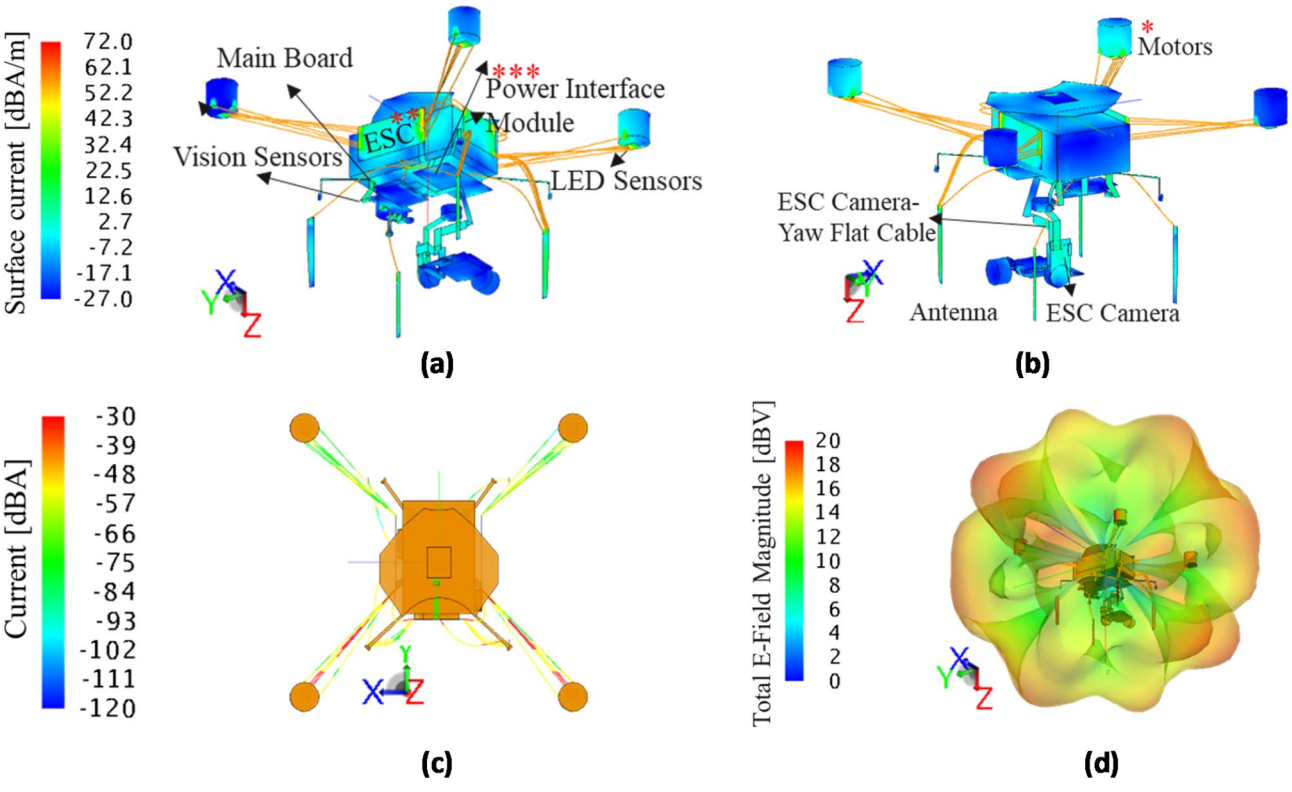

Fig. 8. Surface-current distribution of Mode 10 of the Phantom 4 UAV structure at: 2.47 GHz (a) view 1, (b) view 2, (c) coupled current to the wires, and (d) The radiation pattern of total E-field magnitude.

Antenna	ESC (left, right)	Power interface module	GPS	ESC camera	IMU	Camera	
***	***	***	***	***	***	***	
22	12	11	3	4	4	3	
***	**	**	**	***	***	***	
26	23	8	1	3	2	2	
*	*	*	*	*	*	*	
16	16	11	8	4	3	2	
Motors	Main board	Camera board	LED sensors	Gimball main board	Ultrasonic	GPS cover	Gimball power board
***	***	***	***	***	***	***	***
2	1	1	1	-	-	-	1
***	**	***	***	**	**	**	**
-	3	5	6	1	2	1	1
*	*	*	*	*	*	*	*
9	16	2	-	3	1	2	1

Table 1. The number of vulnerabilities of each subsystem component to EMI in the frequency range of 200 mhz to 5 ghz.

Vision sensors -main board	ESC (L, *R*) - main board	Camera board -ESC camera -Gimball main board	ESC camera - roll	Ultrasonic-main board	Yaw - ESC camera	Pitch-IMU	Camera-IMU	Flight controller-main board
***	***	***	***	***	***	***	***	***
38	8	4	2	2	1	1	-	-
**	**	**	**	**	**	**	**	**
19	1	3	3	3	4	1	1	1
*	*	*	*	*	*	*	*	*
9	2	7	1	-	5	2	1	-

Table 2. The number of vulnerabilities of flat cables connected each subsystem component to EMI in the frequency range of 200 mhz to 5 ghz.

Wires					
Motor-ESC	Main Board-Antenna	Power Interface Module-GPS	LED Sensors-ESC	Power Interface Module-Antenna	Power Interface Module-ESC
37	34	22	15	7	6

Table 3. The number of vulnerabilities of Phantom 4 UAV wires to EMI in the frequency range of 200 mhz to 5 ghz.

The simulation process was refined by segmenting the frequency range into 100 MHz intervals, allowing for precise resonance identification. Figures 7 and 8 illustrate results for mode 9 (2.41 GHz) and mode 10 (2.47 GHz), corresponding to the high-power source frequency (2.45 GHz). The power transfer module exhibited the highest induced current, followed by antennas and ESC boards. Additional subsystems such as the ultrasonic board, main board, gimbal power board, vision sensors, and LED sensors were also significantly affected. Following the identification of resonance frequencies for each mode, the Jn distributions and radiation patterns were plotted for those specific frequencies. The color-coded diagrams indicate the precise distribution of currents, where areas of maximum current are highlighted in red, and areas with zero current are marked in blue. The radiation pattern diagrams further show the directions from which the maximum current distribution on the UAV is expected when exposed to incident waves. Based on this analysis, it is possible to determine which subsystems experience the highest current levels. For example, in Fig. 7, corresponding to mode 9 at 2.41 GHz, the power transfer module exhibits the highest current, marked with ***, followed by the antennas **, and the ESC boards *. Additional subsystems such as ultrasonic board, the main board, gimbal power board, vision sensors, and LED sensors also show significant current levels. Similarly, for mode 10 at 2.47 GHz, as shown in Fig. 8, the power transfer module shows the highest current, followed by the ESC boards and motors. Given the unpredictability of EMI sources in real-world scenarios, a statistical approach was adopted. Table 1 summarize EMI vulnerability across all UAV subsystems over the full frequency range of 200 MHz to 5 GHz. Tables 2 and 3 focuses on wiring, identifying the most affected connections.

Table 1 categorizes the UAV subsystems based on the number of times maximum current distribution was observed across the analyzed frequency range. Table 1 ranks the subsystems based on the frequency of high current

distribution occurrences, categorizing them into three priority levels. The subsystems are ranked according to three priority levels: the first level (three stars) indicates the highest current distribution, the second level (two stars) indicates the second-highest, and the third level (one star) denotes the third priority. The numbers in the table reflect the frequency of maximum current distribution observed for each subsystem. Subsystems frequently displaying maximum current distribution are considered more vulnerable to electromagnetic interference.

Table 2 categorizes flat cables following the same approach used for Table 1. For instance, "vision sensors-main board" represents the flat cable connecting the vision sensor board to the main board, and this pattern applies to all elements listed in Table 2. The table indicates that the flat cable connecting the vision sensors to the main board has the highest current distribution, followed by the antennas and ESC boards in Table 1. A notable characteristic of flat cables is their low susceptibility to noise due to their differential operation. Since these cables measure voltage differentially, common-mode noise is effectively canceled. This property, as further discussed, prevents damage to the vision sensor and main board despite high induced currents.

Table 3 pertains to the wiring, where only the wire with the highest current distribution is noted without applying the three-level ranking system. Among the wires, those connecting the motors to the ESC boards exhibited the highest current distribution.

This comprehensive evaluation provides critical insights into UAV EMI vulnerabilities, offering guidance for future UAV design modifications. Enhanced shielding strategies, particularly for power transfer modules and long wiring connections, can improve UAV resilience in complex electromagnetic environments.

Experimental validation of electromagnetic susceptibility

The methodology of this study involved an initial simulation phase to identify UAV subsystems with the highest induced currents under EMI conditions, followed by experimental validation to determine which of these subsystems were most vulnerable to damage.

A DJI Phantom 4 model was tested in a controlled laboratory environment to assess its performance against high-power electromagnetic fields. Due to limited access to commercial high-power sources, an experimental setup was developed using two commercial magnetron tubes (model 2M246) to create a high-power electromagnetic source. These magnetrons fed into a horn antenna, producing an effective isotropic radiated power (EIRP) of approximately 22 kW at 2.45 GHz. This setup, as illustrated in Fig. 9, was designed to generate a continuous wave (CW) with high intensity, which served as the radiation source for testing the electromagnetic susceptibility of the Phantom 4 UAV.

During testing, the UAV was placed at distances of 3, 2.5, 1.5, 1, and 0.6 m from the electromagnetic source, with performance degradation observed at each distance. The choice of a 3-meter maximum distance was dictated by the power limitations of the electromagnetic source used in the experiment. Beyond this range, the UAV exhibited no noticeable response to the incident electromagnetic field, as the induced interference was insufficient to affect its operation. By progressively decreasing the distance, the signal strength increased and systematically analyze the impact of varying electromagnetic field intensities on UAV performance. This approach helps to evaluate both the effect of signal strength variations and the influence of changing the radiation distance. Table 4 presents the measured field strength and power density at various distances from the electromagnetic source. The field strength values, measured in volts per meter (V/m), indicate the intensity of the electromagnetic field at each distance. As the UAV moves closer to the source, the field strength increases from 272 V/m at 3 m to 1360 V/m at 0.6 m. The power density values, given in watts per square meter (W/m^2), represent the electromagnetic energy received per unit area. Following the inverse-square law, the power density increases significantly as the distance decreases, from 196 W/m^2 at 3 m to 4905 W/m^2 at 0.6 m. These measurements provide crucial insight into the UAV's exposure levels and help explain the observed EMI effects on its subsystems. The results indicate that the entire UAV structure was affected at 3 m, with severity increasing

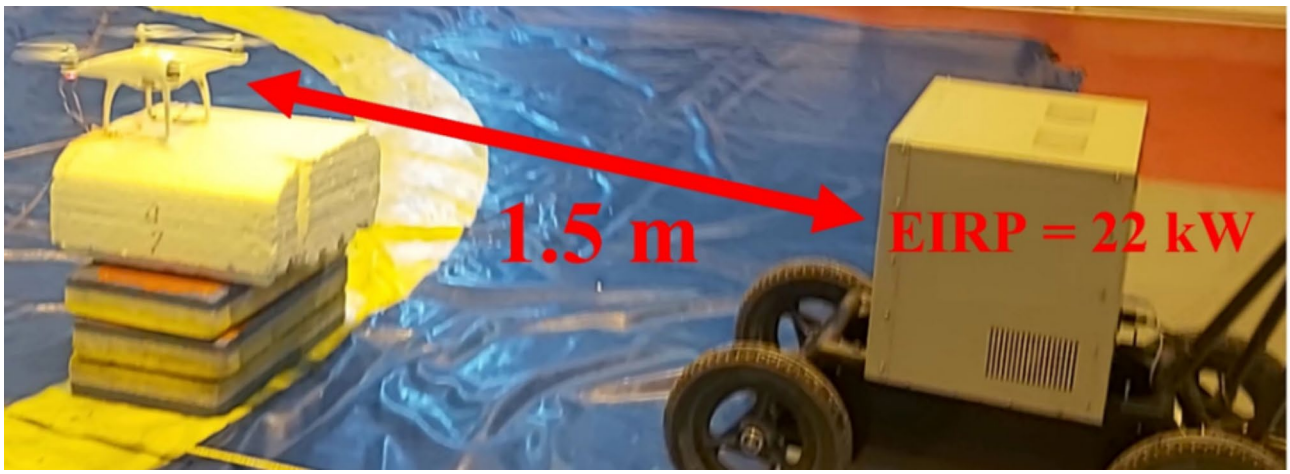

Fig. 9. High-Power Wave Radiation Device Operating at 2.45 GHz with EIRP = 22 kW CW for Phantom Exposure.

Distance	0.6 m	1 m	1.5 m	2.5 m	3 m
Field strength (V/m)	1360	816	544	326	272
Power density (W/m^2)	4905	1766	785	282.5	196

Table 4. Field intensity and power density at various distances from a source with eirp ≈ 22 kw.

Wire type	The number of occurrences of the highest current distribution at different resonance frequencies	Vulnerability
Motor to ESC board	Highest (37)	High
Main board to antennas (coaxial)	High (34)	Low
Power interface module to GPS	Moderate (22)	High

Table 5. Current levels in various wires in the Phantom 4 UAV.

at shorter distances. The motors were identified as the most vulnerable component across all test distances due to their long power wires, which acted as antennas, leading to excessive absorption of electromagnetic energy and motor malfunction. At 0.6 m, both the motors and the GPS board were completely disabled due to the field's intensity.

Based on the experimental results:

- At a distance of 3 m, the entire Phantom 4 structure was affected by the electromagnetic field, with the field impact increasing as the distance decreased to 0.6 m.
- Across all distances, the motors were the most vulnerable component, primarily due to the long power wires connecting the ESC board to the motors. These wires acted as antennas, readily absorbing the surrounding field, leading to motor malfunction.
- At a distance of 0.6 m, both the motors and the GPS board were completely destroyed by the electromagnetic field.

Simulations confirmed that power in EMI environments is primarily coupled through long wires connecting different components. Table 3 highlights that the wires connecting the motors to the ESC boards exhibited the highest current levels, followed by those linking the main board to the antennas and the power interface module to the GPS. The experimental findings support these results, as motor failure was traced to ESC-motor wiring, while GPS malfunction was linked to the power interface module. Coaxial cables connecting the mainboard to antennas, despite showing high current levels, remained operational due to their shielding. These findings are summarized in Table 5. The table provides a summarized assessment of current distribution and vulnerability among UAV components. The wires connecting the motors to the ESC boards exhibited the highest current levels and were also the most susceptible to damage. The coaxial cables between the main board and antennas also showed high current levels but remained less vulnerable due to their shielding. Additionally, the power interface module and GPS board experienced relatively high induced currents, but their lack of shielding made them highly susceptible to EMI-induced failures.

Additionally, differential flat cables exhibited high voltage in some regions but were less affected by EMI due to common-mode noise suppression. These results emphasize that longer power cables are more prone to absorbing and transferring EMI, whereas shorter cables may not induce significant voltage spikes. To improve EMI resilience, additional shielding measures, similar to those used in coaxial cables, should be implemented for longer power supply wires.

Conclusion

This study provides valuable insights into the electromagnetic susceptibility of UAV subsystems, particularly focusing on power supply cables and their role in EMI-induced damage. Through both simulations and experimental validation, the findings suggest that shielding, such as that used in coaxial cables, could be a viable solution for reducing the impact of EMI on critical subsystems. Additionally, differential flat cables demonstrated a higher resilience to EMI due to their ability to suppress common-mode noise.

The vulnerability of long power supply cables, as highlighted in both simulation and real-world testing, underscores the need for enhanced design strategies in future UAV models. To further improve UAV electromagnetic resilience, implementing frequency-selective shielding, optimizing grounding techniques, and integrating EMI-resistant circuit designs should be considered. These findings are not limited to the DJI Phantom 4 but are applicable across various UAV platforms, allowing manufacturers to optimize their designs for environments with unpredictable EMI sources. By addressing these vulnerabilities, UAV designs can be optimized for more robust performance, ensuring greater operational reliability in electromagnetically dense environments.

Data availability

All data generated or analysed during this study are included in this published article.

Received: 2 December 2024; Accepted: 13 March 2025
Published online: 23 March 2025

References

1. Liu, Z., Wang, X. & Liu, Y. Application of unmanned aerial vehicle hangar in transmission tower inspection considering the risk probabilities of steel towers. *IEEE Access.* **7**, 159048–159057 (2019).
2. Kim, S. G., Lee, E., Hong, I. P. & Yook, J. G. Review of intentional electromagnetic interference on UAV sensor modules and experimental study. *Sensors* **22**, 2384 (2022).
3. *Phantom 4 User Manual* (2016).
4. Kim, S. et al. Electromagnetic signature of a quadcopter drone and its relationship with coupling mechanisms. *IEEE Access.* **7**, 174764–174773 (2019).
5. Li, T., Wen, B., Tian, Y., Li, Z. & Wang, S. Numerical simulation and experimental analysis of small drone rotor blade polarimetry based on RCS and micro-Doppler signature. *IEEE Antennas. Wirel. Propag. Lett.* **18**, 187–191 (2018).
6. Compatibility, E., Testing & Techniques, M. Radiated, Radio-Frequency, electromagnetic field immunity test. *Br. Standard EN IEC*, 61000–61004, Part 4-3, (2020).
7. Hamdalla, M. Z. et al. Characteristic mode analysis prediction and guidance of electromagnetic coupling measurements to a UAV model. *IEEE Access.* **10**, 914–925 (2021).
8. Harrington, R. & Mautz, J. Theory of characteristic modes for conducting bodies. *IEEE Trans. Antennas Propag.* **19**, 622–628 (1971).
9. Gao, G., Zhang, R. F., Geng, W. F., Meng, H. J. & Hu, B. Characteristic mode analysis of a nonuniform metasurface antenna for wearable applications. *IEEE Antennas. Wirel. Propag. Lett.* **19**, 1355–1359 (2020).
10. Chen, Y. & Wang, C. F. *Characteristic Modes: Theory and Applications in Antenna Engineering* (Wiley, 2015).
11. Ren, K., Nikkhah, M. R. & Behdad, N. Design of dual-polarized, platform-based HF antennas using the characteristic mode theory. *IEEE Trans. Antennas Propag.* **68**, 5130–5141 (2020).
12. Feng, B., He, X. & Cheng, J. C. Dual-wideband dual-polarized metasurface antenna array for the 5G millimeter wave communications based on characteristic mode theory. *IEEE Access.* **8**, 21589–21601 (2020).
13. Elias, B. B. Q., Soh, P. J., Al-Hadi, A. A., Akkaraekthalin, P. & Vandenbosch, G. A. A review of antenna analysis using characteristic modes. *Ieee Access.* **9**, 98833–98862 (2021).
14. SR, V. K., Venkatesh, T. & Rajanna, P. K. T. In *3rd International Conference on Mobile Networks and Wireless Communications (ICMNWC).* 1–6 (IEEE, 2023).
15. Russo, N. E., Zekios, C. L. & Georgakopoulos, S. V. A CMA-Based electronically reconfigurable Dual-Mode and Dual-Band antenna. *Electronics* **12**, 3915 (2023).
16. Garbacz, R. Modal expansions for resonance scattering phenomena. *Proc. IEEE.* **53**, 856–864 (2005).
17. Harrington, R. & Mautz, J. Computation of characteristic modes for conducting bodies. *IEEE Trans. Antennas Propag.* **19**, 629–639 (1971).
18. Guo, X. Y., Lian, R. Z., Zhang, H. L., Chan, C. H. & Xia, M. Y. Characteristic mode formulations for penetrable objects based on separation of dissipation power and use of single surface integral equation. *IEEE Trans. Antennas Propag.* **69**, 1535–1544 (2020).
19. Ylä-Oijala, P. Generalized theory of characteristic modes. *IEEE Trans. Antennas Propag.* **67**, 3915–3923 (2019).
20. Ethier, J. & McNamara, D. A. The use of generalized characteristic modes in the design of MIMO antennas. *IEEE Trans. Magn.* **45**, 1124–1127 (2009).
21. Obeidat, K. A., Raines, B. D. & Rojas, R. G. Application of characteristic modes and non-foster multiport loading to the design of broadband antennas. *IEEE Trans. Antennas Propag.* **58**, 203–207 (2009).
22. Adams, J. J. & Bernhard, J. T. A modal approach to tuning and bandwidth enhancement of an electrically small antenna. *IEEE Trans. Antennas Propag.* **59**, 1085–1092 (2011).
23. Li, H., Lau, B. K., Ying, Z. & He, S. Decoupling of multiple antennas in terminals with chassis excitation using polarization diversity, angle diversity and current control. *IEEE Trans. Antennas Propag.* **60**, 5947–5957 (2012).
24. Ryan, C. G. & Eleftheriades, G. V. Two compact, wideband, and decoupled meander-line antennas based on metamaterial concepts. *IEEE Antennas. Wirel. Propag. Lett.* **11**, 1277–1280 (2012).
25. Hamdalla, M. Z., Hassan, A. M. & Caruso, A. N. In *2019 IEEE International Symposium on Antennas and Propagation and USNC-URSI Radio Science Meeting.* 1497–1498 (IEEE, 2019).
26. Hunter, J. et al. In *Annual Directed Energy Science and Technology Symposium.*
27. Hamdalla, M. Z., Roacho-Valles, J. M., Caruso, A. N. & Hassan, A. M. Electromagnetic compatibility study of quadcopter UAVs: Characteristic mode analysis of the frame's material and shape effect. *Progress Electromagnet. Res. M,* **112**, 1–14, (2022).
28. Hamdalla, M. Z. et al. In *2019 IEEE International Symposium on Antennas and Propagation and USNC-URSI Radio Science Meeting.* 553–554 (IEEE, 2019).
29. Hamdalla, M. Z., Bissen, B. B., Caruso, A. N. & Hassan, A. M. In *2020 IEEE International Symposium on Antennas and Propagation and North American Radio Science Meeting.* 1799–1800 (IEEE, 2020).
30. https://altair.com/feko (2023).

Author contributions

Z. J. and A. S. conducted the simulations. S. M. H. developed the analysis methodology and validated the simulations. V. M. and J. G. contributed to the analysis of results and experimental measurements. All authors participated in the scientific review of the work and collaboratively wrote the manuscript.

Declarations

Competing interests

The authors declare no competing interests.

Additional information

Correspondence and requests for materials should be addressed to S.M.H.

Reprints and permissions information is available at www.nature.com/reprints.

Publisher's note Springer Nature remains neutral with regard to jurisdictional claims in published maps and institutional affiliations.